Effects of Catalyst Morphology on Oxygen Defects at Ni–CeO$_2$ Interfaces for CO$_2$ Methanation

Effects of Catalyst Morphology on Oxygen Defects at Ni-CeO$_2$ Interfaces for CO$_2$ Methanation †

Samiha Bhat[1], Miguel Sepúlveda-Pagán[2], Justin Borrero-Negrón[2], Jesús E. Meléndez-Gil[2],

Eranda Nikolla[1*], Yomaira J. Pagán-Torres[2*]

[1]Department of Chemical Engineering, University of Michigan, Ann Arbor, MI, United States

[2]Department of Chemical Engineering, University of Puerto Rico-Mayagüez Campus, Mayagüez, PR, United States

*Corresponding authors: erandan@umich.edu, yomairaj.pagan@upr.edu

Abstract

Oxygen defects in Ni-CeO$_2$ catalysts play an important role for CO$_2$ methanation. Herein, efforts are centered on enhancing the concentration of oxygen defects by tuning the Ni-CeO$_2$ catalyst morphology to enhance methane productivity. A relationship between oxygen defect concentration, the structure of Ni-CeO$_2$ catalysts and catalytic performance for CO$_2$ methanation is established through a combination of catalyst characterization (scanning transmission electron microscopy (STEM), temperature programmed reduction (H$_2$-TPR), H$_2$ pulse chemisorption, X-ray diffraction, *in situ* diffuse reflectance infrared Fourier transform spectroscopy (DRIFTS), and Raman spectroscopy) and kinetic studies. Raman studies indicated that (i) inverse Ni-CeO$_2$ catalyst structures, along with (ii) incorporation of low amounts of (< 1 wt%) of aliovalent, rare-earth metal dopants, such as Pr, enhanced the formation of oxygen defects, consequently leading to high methane productivity. *In situ* DRIFTS studies showed that CO$_2$ methanation over Ni-CeO$_2$ inverse catalysts with the best catalytic performance followed a formate reaction pathway.

1. Introduction

The combustion of fossil fuels, including coal, natural gas, and crude oil, has served for decades as the primary global energy source. A significant challenge with these processes is the emission of carbon dioxide (CO_2), with adverse environmental impacts such as ocean acidification and climate change.[1] Substantial efforts have been dedicated to the development of technologies to reverse environmental impacts of CO_2 through CO_2 capturing and conversion into useful products using renewable energy sources.[1,2] Power-to-Gas (Pt-G) conversion has gained significant traction as it involves the synthesis of methane (CH_4), as an energy carrier, through the capture and reduction of CO_2 with renewable hydrogen produced from water electrolysis.[3] Methane is a valuable product with wide applications in the industrial and domestic sectors.[4] Furthermore, NASA uses the CO_2 methanation reaction ($CO_2 + 4H_2 \leftrightarrow CH_4 + 2H_2O$) to produce methane within the Oxygen Generator and Carbon Dioxide Removal Assembly (CDRA) systems on the International Space Station, where H_2 from water electrolysis is used to hydrogenate metabolically produced CO_2 waste from crew members.[5]

CO_2 methanation ($CO_2 + 4H_2 \leftrightarrow CH_4 + 2H_2O$, ΔH_{298K} = -165 kJ/mol) is a highly exothermic reaction, thermodynamically favored at temperatures lower than 400°C. Operation at higher temperatures shifts the thermodynamics toward the formation of CO via the reverse water gas shift reaction ($CO_2 + H_2 \leftrightarrow CO + H_2O$, ΔH_{298K} = 41 kJ/mol). Numerous heterogeneous catalysts have been evaluated for CO_2 methanation over the years, including Ru, Rh, Pd, Ni, and Co supported on various metal oxides.[6–8] In general, supported precious metal catalysts are more active at lower temperatures but are cost prohibitive. Supported Ni catalysts have been reported to provide a compromise between catalytic activity and cost.[6,9] As such, significant effort has been dedicated toward improving the catalytic activity and selectivity of supported Ni catalysts at temperatures lower than 400°C.[3,10–13]

Ni supported on γ-Al_2O_3 is the commercial standard for this reaction.[3] Replacing γ-Al_2O_3 with reducible oxides (CeO_2, ZrO_2, and TiO_2) has been reported to significantly increase the catalytic activity in these systems because of enhanced metal-support interactions through the redox properties of the oxide.[13–16] Among these, Ni-CeO_2 has been reported to exhibit high catalytic activity owing to the reversible redox properties of ceria (Ce^{4+} to Ce^{3+}), which have been demonstrated to play an important role in oxygen mobility, oxygen defect generation, and

adsorption and activation of CO_2.[9,12,17–23] In these catalysts, metallic Ni sites have been associated with facilitating H_2 dissociation, which through spillover induces the formation of defected ceria under reducing conditions, both of which are important for the CO_2 methanation chemistry.[17,20] The effects of Ni metal loading on reducible oxides on the CO_2 methanation mechanism have been reported, however they are often controversial due to limited insights on the nature of the active sites that govern selective methane formation.[12,20,22] In general, studies on supported Ni-catalysts have shown that their performance is influenced by (i) support effects (defect structure, dispersion, morphology, metal-support interactions), (ii) metal dispersion, and (iii) the use of secondary metal promoters.[3,13,24–28]

Supported metal nanoparticles generated from reduced non-stoichiometric mixed metal oxide frameworks belonging to the perovskite family ($A_{n+1}B_nO_{3n+1}$; $n=1, 2, 3… →∞$, A is often a lanthanide, or an alkaline earth metal cations and B is often a transition metal cations) through exsolution have also been investigated for CO_2 methanation.[29] Exsolution leads to close interfaces between the exsolved metal nanoparticles and the restructured parent oxide improving metal-oxide interactions and consequently impacting catalytic performance for this reaction.[29,30] Palkovits and coworkers showed that reduction of $La_{0.5}Ce_{1.5}NiO_4$ oxide resulted in exsolution of well-dispersed Ni nanoparticles at the interface with the oxide with improved CO_2 methanation activity and stability compared to commercial $Ni/\gamma-Al_2O_3$ catalyst. The authors also showed that the methanation pathway on this catalyst structure followed a different route (CO-route) than the conventional formate route on the commercial catalyst, suggesting the formation of a unique metal/metal oxide interface in the exsolved catalyst structures.[30]

In aggregate, independent of the method used to synthesize supported Ni catalysts, literature has suggested that Ni at the interface with redox active oxides has significant potential for CO_2 methanation. However, a debate exists on the nature of the active site and the effect that stems from the redox properties of the oxide and the Ni particle characteristics. Herein, to interrogate these effects, we investigate CO_2 methanation on a series of $Ni-CeO_2$ catalytic systems from conventional to inverse catalyst structures. The inverse $Ni-CeO_2$ structures are used to probe the effects from oxygen defect generation in CeO_2 on CO_2 methanation, since they contain dispersed oxide islands on large Ni nanoparticles. Conversely, conventional supported catalyst systems are characterized by dispersed Ni particles on CeO_2. To further tune the redox properties

of ceria at the interface with Ni, we have also incorporated aliovalent promoters at 1 wt% (Gd, La, Pr) and investigated their impact on the concentration of oxygen vacancies and catalytic performance.

2. Experimental

2.1. Materials and catalyst synthesis methods

A series of catalysts with different Ni loadings (X wt% Ni-CeO$_2$, X = 5, 15, 40, 60, 70) were prepared by a co-precipitation method. In a typical synthesis, appropriate amounts of Ce(NO$_3$)$_3$·6H$_2$O (Sigma Aldrich – 392219) and Ni(NO$_3$)$_2$·6H$_2$O (Alfa Aesar – AAA1554022) were dissolved in 100 of ethanol (Fisher Scientific – A692P-4). Subsequently 75 mL of 0.5 M oxalic acid (Sigma Aldrich – 194131) was added dropwise to the precursor solution and the slurry was aged for 1 h under vigorous stirring. A precipitate was formed during the aging process. The precipitated solution was then centrifuged at 5,000 rpm for 5 min, washed 5 times with deionized water, followed by a final wash with ethanol. Lastly, the solution was transferred to a ceramic crucible and dried overnight in a convection oven at 120°C. The obtained metal-oxide powder was then calcined at 400°C for 3 h at a ramp rate of 5°C/min while being exposed to air at a flowrate of 40 mL/min. A series of 60 wt% Ni-CeO$_2$ catalysts doped with 1 wt% rare-earth metals, denoted as 60 wt% Ni 1 wt% M-CeO$_2$ (M = Pr, La, Gd), were also synthesized following a similar co-precipitation synthesis route. Appropriate amounts of metal precursor salts of Pr(NO$_3$)$_3$·6H$_2$O (Alfa Aesar AAA1290909), La(NO$_3$)$_3$·6H$_2$O (Alfa Aesar AAA1291522) and Gd(NO$_3$)$_3$·6H$_2$O (Alfa AesarAAA1291722) were stirred along with the Ce(NO$_3$)$_3$·6H$_2$O and Ni(NO$_3$)$_2$·6H$_2$O salts in 100 mL of ethanol to form precipitates. Similar washing and calcination steps were followed as the procedure described above for the X wt% Ni-CeO$_2$ catalysts.

Unsupported Ni catalyst and CeO$_2$ support were synthesized by dissolving 7.5 g of Ni(NO$_3$)$_2$.6H$_2$O and 10 g of Ce(NO$_3$)$_3$.6H$_2$O respectively in 100 mL of ethanol. A 75 mL of 0.5 M oxalic acid solution served as the precipitating agent and was added dropwise to the solution under continuous stirring. The unsupported Ni catalyst and CeO$_2$ support were obtained following the same steps of centrifugation, washing, drying, and calcining as detailed above for X wt% Ni-CeO$_2$ catalysts.

2.2. Catalyst characterization

The bulk structure, morphology, Ni particle size and loading, reducibility, and interfacial properties of the CeO_2 support, unsupported Ni and Ni-CeO_2 catalysts were characterized by X-ray diffraction, N_2 physisorption, inductively coupled plasma-optical emission spectrometry (ICP-OES), scanning transmission electron microscopy (STEM), H_2 pulse chemisorption, H_2 temperature-programmed reduction (H_2-TPR) and Raman spectroscopy. Prior to the characterization studies, all catalysts were reduced at 425°C (ramp rate of 5°C/min) for a dwell time of 4 h while being exposed to a H_2 flow at 40 mL/min.

Powder X-ray diffraction (XRD) patterns were acquired on a Rigaku Smartlab XRD equipped with a D/tex ultra 250 high speed silicon strip 1D detector at 40 kV and 44mA using Cu-Kα (λ = 0.15406 nm) radiation and a shape factor (k) of 0.9.[31] The scan range was fixed with 2θ values between 20° and 80° with an incremental step angle of 2°/min. The Brunauer–Emmett–Teller (BET) specific surface areas (m^2/g) were determined from the N_2 adsorption-desorption isotherms at 77 K, using a Micromeritics ASAP 2020 adsorption analyzer. All samples (100 mg) were degassed at 300°C for 180 minutes prior to analysis to remove volatiles and other adsorbed species before analysis. Elemental analysis of Ni, Pr, Gd, and La for the as-synthesized catalysts were determined using ICP-OES performed by Galbraith Laboratories, Inc.

HAADF-STEM (High-angle annular dark-field scanning transmission electron microscopy) micrographs were obtained on a 200 kV FEG scanning transmission electron microscope (Thermo Fisher Talos F200X G2) at the MC^2 characterization facility at the University of Michigan, Ann Arbor. EDS (Energy-dispersive X-ray spectroscopy) mapping of Ni and Ce particles at three different spots were obtained by performing repeated elemental scans on one spot for 10 – 15 minutes with a dwell time of 1μs per scan. The 15 and 60 wt% Ni-CeO_2 samples were prepared by crushing and dispersing 1.5 mg of the sample in 2 mL of isopropanol with continuous sonication for an hour. The dispersions were then dropped onto holey carbon coated Cu grids and dried for 2 hours before imaging. The samples were also plasma cleaned using a Gatan Solarus II Plasma Cleaning System to remove any impurities before imaging. Caution was taken to prevent destruction of the sample under intense beam conditions at higher magnifications and images reported herein are based on consistent observations over 5 different areas per sample. Raman spectra were taken with Thermo Scientific DXR Raman Microscope using a 5 mW powered 532 nm laser with an exposure time of 4 seconds and the data was averaged for 16 exposures. The data

was baseline corrected to obtain the raw intensities for the F_{2g} and D_1 peaks for a quantitative understanding of the features observed.

H_2-TPR and H_2 pulse chemisorption were conducted in a Micromeritics Autochem 2920 II equipped with a TCD filament and U-tube reactor within a furnace. In a typical TPR experiment, 50-60 mg of a sample was loaded into a quartz U-tube reactor and calcined at 400°C (ramp of 10°C /min). The H_2-TPR measurements were taken flowing a 5% H_2/Ar mixture over the catalyst at 50 mL/min while heating from 35-900°C.

Ni dispersion (D_{Ni}) was evaluated using H_2 pulse chemisorption experiments.[17] Typically, 50-60 mg of the sample loaded in the U-tube reactor was first reduced in-situ at 425°C (ramp of 5°C/min) for 1 h under 5% H_2/Ar mixture at a flow rate of 50 mL/min, cooled to ambient temperature under an inert atmosphere (Ar) and later pulse injected with H_2 at a stable temperature of 35°C until saturation was reached. The adsorption stoichiometry factor (SF) of Ni/H_2 was assumed to be 2 and the Ni dispersion (D_{Ni}) was calculated with the following equation.

$$D_{Ni}(\%) = \frac{SF \times V_{H_2} \times MW_{Ni}}{m_{cat} \times w_{Ni}} \times 10^4 \qquad (1)$$

Where SF = 2 is the stoichiometric factor, V_{H_2} is the cumulative volume of H_2 adsorbed until saturation (mmol), MW_{Ni} is the molecular mass of Ni (58.71 g/mol), m_{cat} is the mass of the catalyst weighed for analysis in the U-tube (g), w_{Ni} is the weight loading Ni (%) in the synthesized catalyst as determined from ICP-OES elemental analysis.

In situ diffuse reflectance infrared Fourier transform spectroscopy (DRIFTS) studies were performed on a Nicolet IS10 FTIR spectrometer equipped with MCT detector. A high temperature reaction chamber equipped with ZnSe windows mounted on a Praying Mantis™ attachment (Harrick Scientific Products Inc.) was used for CO_2 methanation studies. For CO_2 methanation studies, 140 mg of catalyst mixed with KBr (KBr/catalyst = 10) was reduced *in situ* at 425°C using a ramp of 10°C/min and 1 h hold under a 50 mL/min flow of 20% H_2/N_2 gas mixture. After reduction the sample was purged with 40 mL/min N_2 for at 425°C; subsequently, the sample temperature was lowered to the analysis temperature (275°C) and a background spectrum was taken. Subsequently, a gas feed mixture comprised of 8% CO_2/ 32% H_2/ 60% N_2 was flowed to

the chamber at a flow rate of 50 mL/min. Spectra were collected while flowing the feed gas mixture at a wavelength range of $800 - 4000$ cm^{-1}.

2.3. Catalytic Performance

Catalytic studies on CO_2 methanation were conducted in a fixed-bed up-flow tubular reactor (5.5 mm internal diameter) (FBR) at atmospheric pressure. The reactor was loaded with 100 mg of catalyst diluted with SiC at a 1:3 ratio (catalyst:SiC) and the catalyst bed was held in place using quartz wool. The temperature of the catalyst bed was monitored and controlled using a type J thermocouple connected to an Oaktron Digisense 9500 temperature controller. Prior to the CO_2 methanation reaction, catalysts were reduced *in situ* at 425°C (5°C/min ramp, 4 h hold) under a flow of H_2 at 40 mL/min. After reduction the reactor was cooled down to the desired reaction temperature between 200°C – 275°C under H_2 flow. A mixture of the reaction gases (10 vol% CO_2, 40 vol% H_2, balance N_2) was then introduced to the reactor at a flowrate of 50 mL/min using mass flow controllers (Brookes Instrument SLA5800). Inlet and outlet gas concentrations were analyzed by an on-line gas chromatograph (Shimadzu GC-2014) equipped with Hayesep-T (80/100 mesh), Hayesep-Q (80/100 mesh), MSieve 5A (60/80 mesh) and Hayesep-D (80/100 mesh) columns. The separated gases were analyzed using a thermal conductivity detector (TCD) and a flame ionization detector (FID) with methanizer. The data reported for the catalytic studies corresponds to the average of four individual sample measurements. The CO_2 conversion (X_{CO_2}), CH_4 selectivity (S_{CH_4}), and CO selectivity (S_{CO}) for each sample taken were determined using the following equations.

$$X_{CO_2}(\%) = \frac{[CO_2]_{in} - [CO_2]_{out}}{[CO_2]_{in}} \times 100 \qquad (2)$$

$$S_{CH_4}(\%) = \frac{[CH_4]_{out}}{[CO_2]_{in} - [CO_2]_{out}} \times 100 \qquad (3)$$

$$S_{CO}(\%) = \frac{[CO]_{out}}{[CO_2]_{in} - [CO_2]_{out}} \times 100 \qquad (4)$$

Methane productivity per catalyst mass was determined using the following equation.

$$\text{Methane productivity (mol g}_{cat}^{-1} \text{ s}^{-1}) = \frac{\text{Moles of methane produced (mol s}^{-1})}{\text{Mass of catalyst (g}_{cat})} \qquad (5)$$

Kinetics studies to determine activation energies were conducted under differential reactor conditions within a temperature range of 200 – 275°C, atmospheric pressure, and using a reaction gas mixture of 10 vol% CO_2, 40 vol% H_2, balance N_2. The gas hourly space velocity (GHSV) varied to obtain CO_2 conversions below 15%. The methane formation rate from catalytic studies was normalized with respect to the cumulative volume of H_2 adsorbed until saturation (V_{H_2}) determined from H_2 pulse chemisorption.

3. Results and discussion

3.1. Catalyst characterization

The XRD patterns of CeO_2 and $Ni-CeO_2$ catalysts with varying Ni loadings synthesized by coprecipitation (from 5 wt% to 70 wt% Ni) post *ex-situ* reduction at 425°C are shown in Fig. 1a. Diffraction peaks corresponding to the (111), (200), (220), (311), and (331) planes of a fluorite-structured CeO_2 are present in all samples.[12] A decrease in peak intensities and changes in peak broadness are observed for ceria as the Ni loading in the catalyst increases (zoom in spectra for the catalyst with low Ni loadings (5 and 15 wt%) are shown in (Fig. S1 †)), due to (i) a decrease in ceria content and (ii) also potentially to generation of mixed crystalline/amorphous phases of ceria as the catalyst structure changes. In addition, diffraction peaks corresponding to the (111), (200), (220) planes of Ni^0 are observed for the catalysts with higher than 15 wt% Ni loading.[21,32] The increase in the intensity of Ni^0 diffraction peaks with Ni loading is associated to the presence of large Ni crystallites (~20 nm). The average Ni crystallite size was determined from the Scherrer equation (Fig. S2 †) and is consistent with the corresponding size distribution histogram (Fig. S3a †) obtained for the 60 wt% $Ni-CeO_2$ catalyst. High-angle annular dark-field scanning transmission electron microscopy (HAADF-STEM) coupled with energy dispersive X-ray spectroscopy (EDS) elemental mapping was employed to characterize the structure of 60 wt% $Ni-CeO_2$ and 15 wt% $Ni-CeO_2$ (Fig. 1b-e). For the 60 wt% $Ni-CeO_2$, dispersed ceria islands on Ni particles are observed consistent with an inverse catalyst structure (Fig. 1b-c). These observations coupled with the XRD results suggest that $Ni-CeO_2$ catalysts with high Ni loading (40 (Fig. S4 †), 60 and 70 wt% Ni) result in the formation of inverted catalyst structures, where ceria islands are supported on Ni particles. Whereas EDS mapping of 15 wt% $Ni-CeO_2$ (Fig. 1d-e) shows dispersed Ni particles supported on CeO_2, which is similar to the structure of conventional supported catalytic materials.
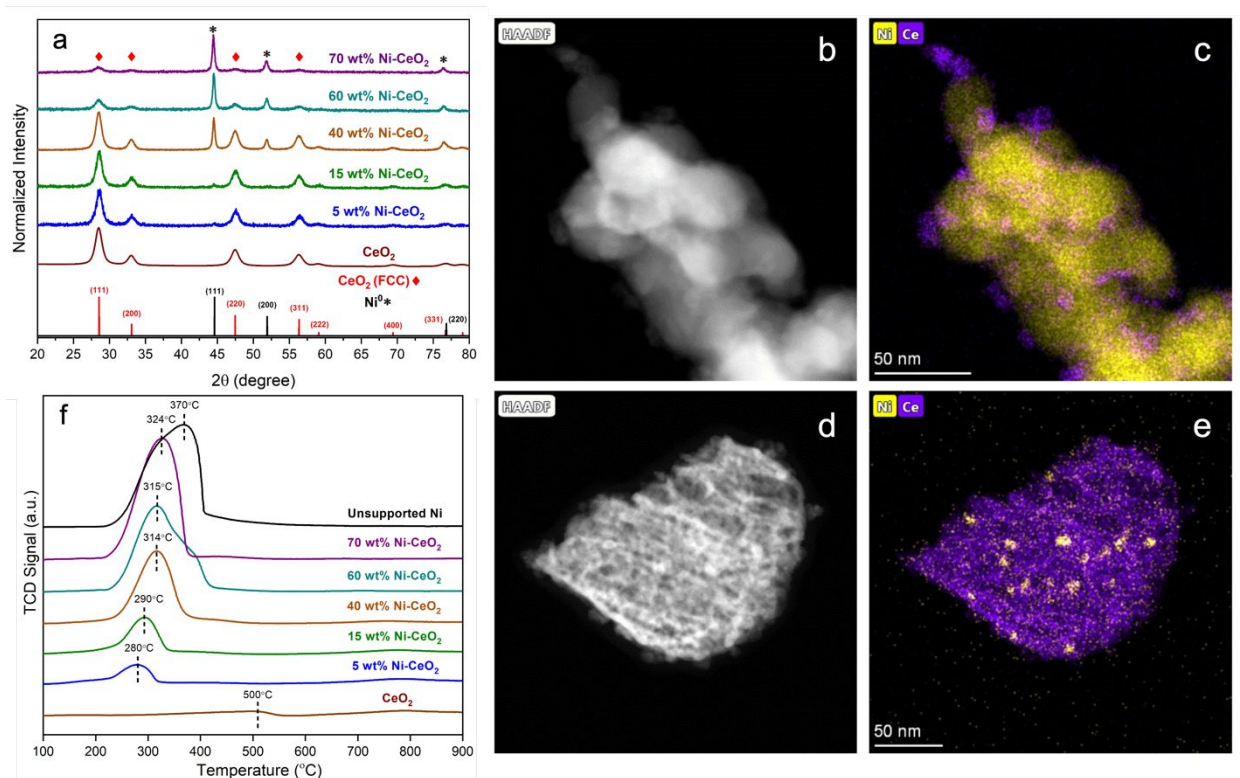
Fig 1. (a) XRD patterns of Ni-CeO$_2$ catalysts. HAADF-STEM images and EDS elemental mapping of (b-c) 60 wt% Ni-CeO$_2$ and (d-e) 15 wt% Ni-CeO$_2$. (f) H$_2$-TPR profiles for Ni-CeO$_2$, unsupported Ni, and CeO$_2$.

The reductive behavior of the supported and inverse catalysts calcined *in situ* at 400°C was studied through H$_2$ temperature programmed reduction studies (H$_2$-TPR) (Fig. 1f). The reduction profile for the unsupported Ni catalyst is characterized by a peak at ~370°C, which is associated with direct reduction of Ni^{2+} to Ni^0 in large Ni crystallite particles.[33] CeO$_2$ exhibited a reduction peak at ~500°C. The Ni-CeO$_2$ catalysts exhibited main reduction peaks between 250-425°C. This reduction peaks appears at ~280°C for the catalyst with the lowest Ni content (5 wt% Ni-CeO$_2$), and gradually increases in intensity and shifts to higher temperatures with an increase in the Ni content in the catalyst. The width of the reduction peak also increases with an increase in Ni content potentially due to (i) an increase in NiO crystallite size, and/or (ii) enriched Ni-CeO$_2$ interactions.[32,34,35] The higher temperature shouldering, characteristic of the 60 wt% Ni-CeO$_2$ catalyst, implies potentially a dominating effect from NiO species interacting with ceria. This is consistent with the metal-metal oxide interactions impacting the reduction temperatures of NiO species reported in the literature.[34–36] The absence of this feature in the catalyst with the highest Ni loading (70 wt% Ni-CeO$_2$), could stem from the reduced interactions between NiO and ceria

due to a decrease in ceria content. The 70 wt% Ni-CeO$_2$ catalyst closely resembles the unsupported Ni with limited NiO-CeO$_2$ interfacial interactions.

The BET surface areas (m^2/g$_{cat}$) (Table 1, Entries 2-6) of the Ni-CeO$_2$ catalysts were determined via N$_2$ physisorption and are largely in the range of 24-45 m^2/g. All catalysts displayed a type IV isotherm (Fig. S5 †). Generally, a decrease in BET surface area is observed as the structure changes from supported to inverted, consistent with a decrease in the amount of ceria in the structure. Table 1 summarizes the Ni loadings determined by ICP-OES for Ni-CeO$_2$ catalysts, along with the Ni dispersion (%) obtained from H$_2$ chemisorption studies. Table 1 shows that the Ni dispersion decreases with increasing Ni loading for Ni-CeO$_2$ catalysts. This is consistent with the large Ni crystallites/particle size observed by XRD and HAADF-STEM imaging.

Table 1. Compositional and physical properties of Ni-based catalysts. The error was generated by running experiments on at least two independent samples.

Entries	Catalyst	Ni Loading[a] (wt %)	Dopant Loading[a] (wt %)	Ni dispersion[b] (%)	BET Surface Area[c] (m^2/g$_{cat}$)
1	CeO$_2$	-	-	-	55 ± 3
2	5 wt% Ni-CeO$_2$	6.4	-	6.8	45 ± 3
3	15 wt% Ni-CeO$_2$	16.3	-	3.8	42 ± 3
4	40 wt% Ni -CeO$_2$	41.6	-	1.2	31 ± 3
5	60 wt% Ni-CeO$_2$	60.3	-	0.7	24 ± 5
6	70 wt% Ni-CeO$_2$	69.1	-	0.7	26 ± 3
7	60 wt% Ni 1 wt% Pr-CeO$_2$	60.8	0.68	0.8	29 ± 3
8	60 wt% Ni 1 wt% Gd-CeO$_2$	62.9	0.70	0.8	26 ± 4
9	60 wt% Ni 1 wt% La-CeO$_2$	63.4	0.72	0.7	16 ± 3

[a] Determined by ICP-OES. [b] Calculated from H$_2$ chemisorption analysis. [c]N$_2$ physisorption BET surface area.

3.2. Supported versus inverse Ni-CeO$_2$ catalysts

3.2.1. Catalytic performance in CO$_2$ methanation

The influence of the different Ni-CeO$_2$ interfaces on the catalytic performance for CO$_2$ methanation in supported (5 wt% and 15 wt% Ni-CeO$_2$) and inverse catalytic structures (40 wt%, 60 wt%, and 70 wt% Ni-CeO$_2$) is shown in Fig. 2a. Similar trends were observed if methane productivity is normalized with respect to μmoles of H$_2$ adsorbed based on H$_2$ pulse chemisorption (Fig. S6 †). All catalysts depicted a steady increase in CO$_2$ conversions with increasing temperatures from 200 – 275°C (Fig. S7 †). Fig. 2a shows that the CO$_2$ conversion and methane productivity at 275°C followed a volcano type behavior with an increase in the Ni content in the catalyst. The inverse 60 wt% Ni-CeO$_2$ showed the highest CO$_2$ conversion (75%) and methane productivity compared to the 15 wt% Ni-CeO$_2$ supported catalyst. Increasing the Ni loading beyond 60 wt% resulted in a decrease in CH$_4$ production possibly due to a decrease in catalytically active Ni-CeO$_2$ interfaces.[34] The Ni-CeO$_2$ interface is critical for CO$_2$ methanation chemistry as highlighted by the fact that the unsupported Ni catalyst resulted in a CO$_2$ conversion of 5% and CH$_4$ selectivity of 15%. Furthermore, subjecting the unreduced best performing inverse catalyst (60 wt% Ni-CeO$_2$) to identical reaction conditions at 275°C also resulted in inferior catalytic performance with a drop in both CO$_2$ conversion and methane productivity (Fig. S8 †), demonstrating that a reduced catalyst prior to testing is critical for achieving high catalytic performance. The superior catalytic performance of the inverse, reduced 60 wt% Ni-CeO$_2$, therefore, can be linked to the redox properties of dispersed ceria at the interface with reduced Ni. Stable performances of the supported (15 wt%) and inverse (60 wt%) Ni-CeO$_2$ catalysts were observed at 250°C for ~20 hours (Fig. S9 †), suggesting insignificant catalyst deactivation over time on stream independent of the catalyst structure.

3.2.2. Characterization of oxygen vacancies

Raman studies for Ni-CeO$_2$ and CeO$_2$ were conducted to probe changes in the defective structure of ceria as a function of Ni loading (Fig. 2b). The Raman shift at 450 cm^{-1} labeled as the F$_{2g}$ band represents the asymmetric stretch of the oxygen anions around a Ce ion and corresponds to the octahedral vibrational modes of the cubic fluorite structure of CeO$_2$.[33,37] This is consistent with the cubic fluorite structure identified by XRD for CeO$_2$. In the case of the Ni-CeO$_2$ catalysts,

in addition to the F_{2g} band, another Raman band at 580 cm^{-1} is observed (Fig. 2b). The Raman band at 580 cm^{-1}, labelled as D_1, has been associated to the structural perturbation of ceria cubic lattice resulting from oxygen defects induced by a redox transition from Ce^{4+} to Ce^{3+}.[21] In addition, slight red shifts of the F_{2g} band are observed in the case of inverse catalysts as the Ni metal content increases from 40 wt% to 70 wt% (Fig. 2b), which literature has attributed to an expansion in the ceria lattice induced by an increase in oxygen vacancies.[17,38] These oxygen vacancies are hypothesized to originate from the dispersed nature of ceria at a close interface with Ni in the inverse catalytic structures. For the supported catalysts (5 and 15 wt% Ni-CeO$_2$), no measurable red shifts of the F_{2g} band were observed in agreement with the literature.[39]
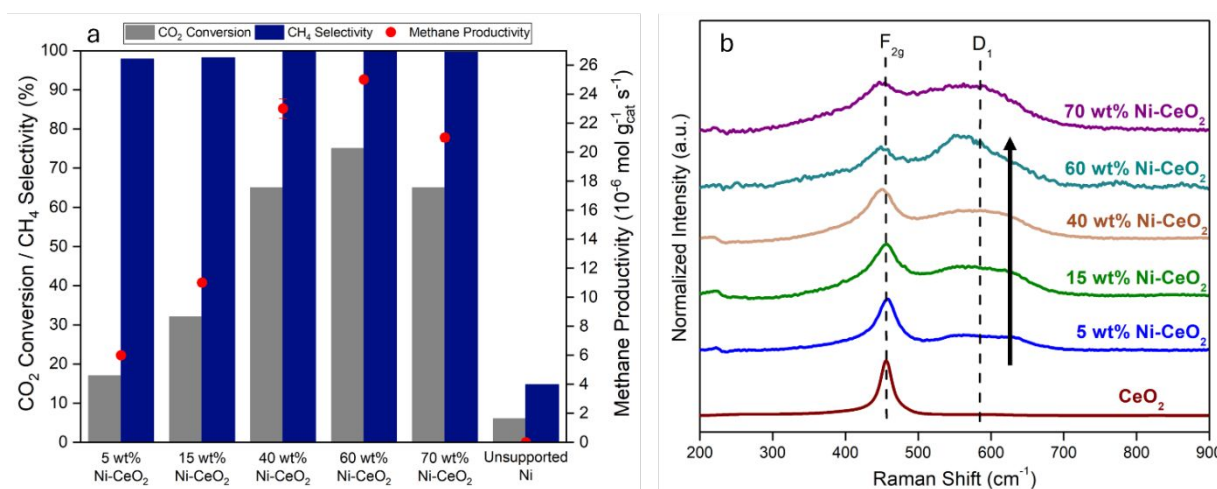

Fig 2. (a) CO_2 conversion/CH_4 selectivity and methane productivity (secondary y-axis) of supported and inverse Ni-CeO$_2$ catalyst in CO_2 methanation. Reaction conditions: P = 1 atm, GHSV = 15,000 mL $g_{cat}^{-1}h^{-1}$, T = 275 ℃, H_2/CO_2 = 4. (b) Raman spectra for supported and inverse Ni-CeO$_2$ catalysts.

The intensity ratio of D_1 to F_{2g} band (I_{D1}/I_{F2g}) has been used in the literature for quantitative analysis of the oxygen vacancy concentration induced by perturbations in the ceria lattice.[37] The ratio of the intensities for D_1 and F_{2g} peaks is shown in Table S1 † (entries 1-5) and plotted as a function of catalyst composition in Fig. S10 † . Fig. S10 † shows a volcano relationship between the D_1/F_{2g} ratios and Ni catalyst loading in Ni-CeO$_2$ catalysts, which follows a similar trend to methane productivity as a function of catalyst composition (Fig. 2a). The 60 wt% Ni-CeO$_2$ catalyst shows the highest I_{D1}/I_{F2g} ratio and methane productivity among the various catalyst compositions. The reduction in D_1/F_{2g} ratio (Fig. S10 †) and methane productivity (Fig. 2a) for the 70wt% Ni-CeO$_2$ catalyst is consistent with the decrease in the Ni-CeO$_2$ interfacial interactions as the ceria

content in the catalyst decreases. These results suggest that oxygen vacancies in ceria play an important role in the catalyst performance for CO_2 methanation.

3.3. Effect of rare-earth metal dopants in Ni-CeO$_2$

3.3.1. Catalyst characterization and performance in CO$_2$ methanation

Aliovalent doping in metal oxides has shown to increase the entropy of metal oxide structures, thus lowering the required oxygen vacancy formation energy. It is known that interstitial incorporation of a dopant into the host metal oxide, such as CeO_2, can result in the substitution of Ce^{4+} with an aliovalent dopant.[38] This substitution leads to a charge imbalance within ceria which is compensated by the formation of oxygen vacancies to maintain charge neutrality at the surface of the metal oxide.[40–42] Herein, the best performing CO_2 methanation catalyst, 60 wt% Ni-CeO$_2$, was modified with low weight loadings (< 1 wt%) of Pr, Gd, and La to probe the effect of oxygen vacancy formation using low-valence metal dopants.

The BET surface areas, metal loadings, and Ni dispersion for doped 60 wt% Ni-CeO$_2$ catalysts are shown in Table 1 (Entries 7-9). The 1 wt% Pr, Gd, and La doped catalysts analogous to their undoped counterpart (60 wt% Ni-CeO$_2$), sustain a type IV isotherm (Fig. S11 †). Additionally, the Ni dispersion (0.7 – 0.8%) remains unaffected after promoting the inverse 60 wt% Ni-CeO$_2$ catalyst with <1 wt% Pr, Gd, or La. The XRD profiles for the doped 60 wt% Ni-CeO$_2$ (Fig. S12a †) show that the incorporation of promoter did not result in changes in Ni particle size based on Scherrer analysis of the (111) and (200) Ni peaks (Fig. S12b †). Analysis of the ceria XRD features are not as conclusive given the broad nature of these peaks induced by the low concentration of ceria and potentially mixed amorphous/crystalline phases of ceria in these reverse catalysts. The H$_2$-TPR profiles for 60 wt% Ni-CeO$_2$ doped with rare-earth metals (Fig. S13 †) show a change in (i) the main reduction peak of Ni^{2+} to Ni^0 to a higher temperature as the dopant is changed from Gd (318℃) to La (326℃) to Pr (338℃), (ii) a higher degree of shouldering of this peak at higher temperature as the dopant is changed from Gd to La to Pr and (ii) a low intensity broad peak centered at ~440°C, which decreases in intensity as the dopant is change from Gd to Pr. These observations suggest that the dopant induced changes at the interface between Ni-ceria, given that the Ni particle size and dispersion was not affected.

The CO_2 methanation performance of doped 60 wt% Ni-CeO_2 (< 1 wt% Pr, La, and Gd) is shown in Fig. 3a. Similar trends were observed if methane productivity is normalized with respect to μmoles of H_2 adsorbed based on H_2 pulse chemisorption (Fig. S14 †). All catalysts depicted a steady increase in CO_2 conversions with increasing temperatures from 200 – 275°C (Fig. S15 †). Among these catalysts, 60 wt% Ni 1 wt% Pr-CeO_2 catalyst resulted in the highest CO_2 conversion (50%) and methane productivity at a reaction temperature of 250°C. The observed enhancement in the CO_2 methanation activity of 60 wt% Ni 1 wt% Pr-CeO_2 is hypothesized to stem from changes in the oxygen defects in ceria through structure doping with Pr at the interface with Ni.[20,38,43] While dopant incorporation in the Ni structure cannot be fully excluded, given the large particle size of Ni and high loading in these catalysts, this effect on the catalytic performance would be significantly more limited than in the case of the dopant incorporating and affecting the defect structure of the highly dispersed ceria. Nevertheless, additional studies are required to conclusively determine the extent, if any, of the dopant incorporation in the Ni structure. The effect of the extent of catalyst reduction was also probed by varying the in-situ reduction temperature from 425°C versus 460°C of the doped catalysts (i.e., 60 wt% Ni 1 wt% Gd-CeO_2) on the catalytic performance and showed limited effect as detailed in Fig. S16†, indicating that the low intensity broad peak centered at ~440°C in the H_2-TPR profile (Fig. S13†) had negligible influence on the catalytic activity of the Gd doped 60 wt% Ni-CeO_2 catalysts. Based on these results, we hypothesize that in the doped inverse catalysts, Ni assists with H_2 dissociating, whereas the Pr, La, or Gd defected ceria contributes to the adsorption and activation of CO_2 at the interface with Ni.

3.3.2. Characterization of oxygen vacancies

Raman spectra for the 60 wt% Ni-CeO_2 catalysts doped with Pr, La, and Gd are shown in Fig. 3b. As discussed above, the undoped 60 wt% Ni-CeO_2 is characterized by two main Raman bands at approximately 450 cm^{-1} and 580 cm^{-1} referred to as F_{2g} and D_1, respectively. Intensity ratios for the D_1 and F_{2g} peaks as a function of the dopant are shown in Table S1 † (entries 6-8). The improved methane productivities for the La and Pr doped 60 wt% Ni-CeO_2 catalyst scale with the oxygen defect concentration, as evidenced from the I_{D1}/I_{F2g} ratios. A ~46% increase of this ratio correlates to a ~42% increase in methane productivity for the best performing 60 wt% Ni 1 wt% Pr-CeO_2 when compared to undoped 60 wt% Ni-CeO_2 (Table S1 †). The enhancement in the defect structure of ceria with aliovalent dopants is consistent with literature reports which have

shown that the addition of low valence metals, such as Pr^{3+}, in the ceria lattice results in the substitution of the host oxide Ce^{4+} ions, creating an electron-deficient surface. This charge imbalance is compensated by the generation of oxygen vacancies in the doped ceria structure.[41,43–46]
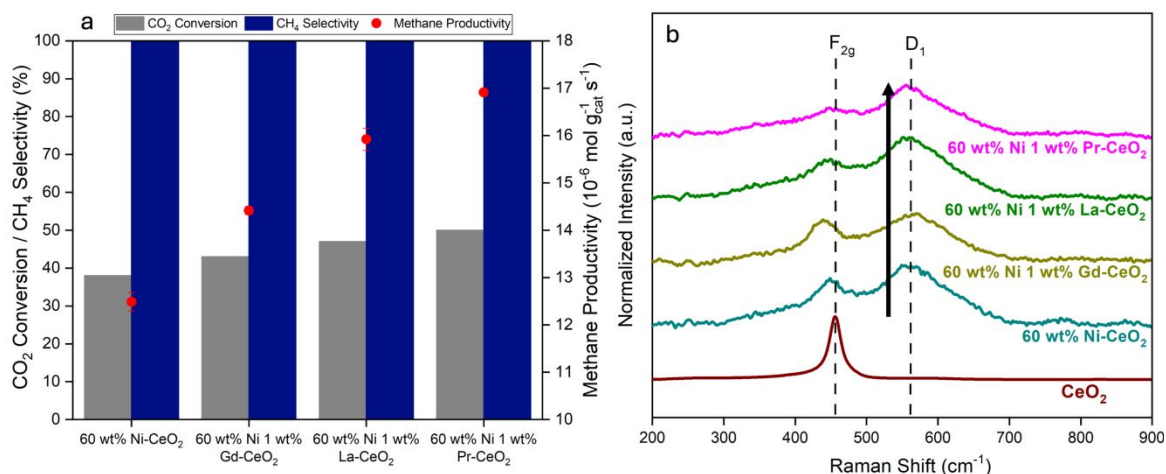

Fig 3. (a) CO_2 conversion/CH_4 selectivity and methane productivity (secondary y-axis) of 60 wt% Ni 1 wt% (Gd, La or Pr)-CeO_2. Reaction conditions: P = 1 atm, GHSV = 15,000 mL $g_{cat}^{-1}h^{-1}$, T = 250 °C, H_2/CO_2 = 4. (b) Raman spectra for 60 wt% Ni 1 wt% (Gd, La or Pr)-CeO_2.

3.4. CO_2 methanation kinetics and proposed mechanism

Kinetic measurements under differential reactor conditions were conducted to obtain apparent activation energies (E_A) for CO_2 methanation over 15 wt% Ni-CeO_2, 60 wt% Ni-CeO_2, and 60 wt% Ni 1 wt% Pr-CeO_2 catalysts (Fig. S17 †). The apparent activation energies for CO_2 extracted from the corresponding Arrhenius plots over these catalysts were in the 108 – 111 kJ/mol range, which is consistent with the range reported in literature.[21] These results indicate that the nature of active sites in Ni-CeO_2 is similar and the differences in the rates mainly arise from the differences in the number of active sites at the Ni-ceria interface, which scales with the concentration of oxygen defects in ceria. Intermediate species formed during CO_2 methanation were qualitatively analyzed through *in situ* DRIFTS studies at 250°C to shed light on the mechanism of the reaction over Ni-CeO_2 catalysts (Fig. 4). The *in situ* DRIFTS spectra show that the predominant reaction intermediates identified over the various Ni-CeO_2 catalysts are bidentate carbonates (b-CO_3) (~1580-1590 cm^{-1} and 1270-1300 cm^{-1}), formates (HCOO) (1500-1510 cm^{-1}

and 1370-1385 cm^{-1}), formyl species (CHO) (~1700-1800 cm^{-1}) and methoxy species (OCH_3) (1060 - 1080 cm^{-1}).[14,47,48] The supported 5 and 15 wt% $Ni-CeO_2$ show limited formation of formyl intermediate species consistent with their lower CH_4 yield obtained in FBR reactor studies when compared to inverse 60 wt% Ni/CeO_2 and doped 60 wt% Ni 1 wt% $Pr-CeO_2$. Conversely, the inverted catalyst structures (40 wt% and 60 wt% Ni/CeO_2 undoped and doped with Pr) show higher extent of formyl intermediates formed. Changes in the concentration of formyl species as a function of catalyst structure and temperature suggest that they play an important role in the CO_2 methanation mechanism.
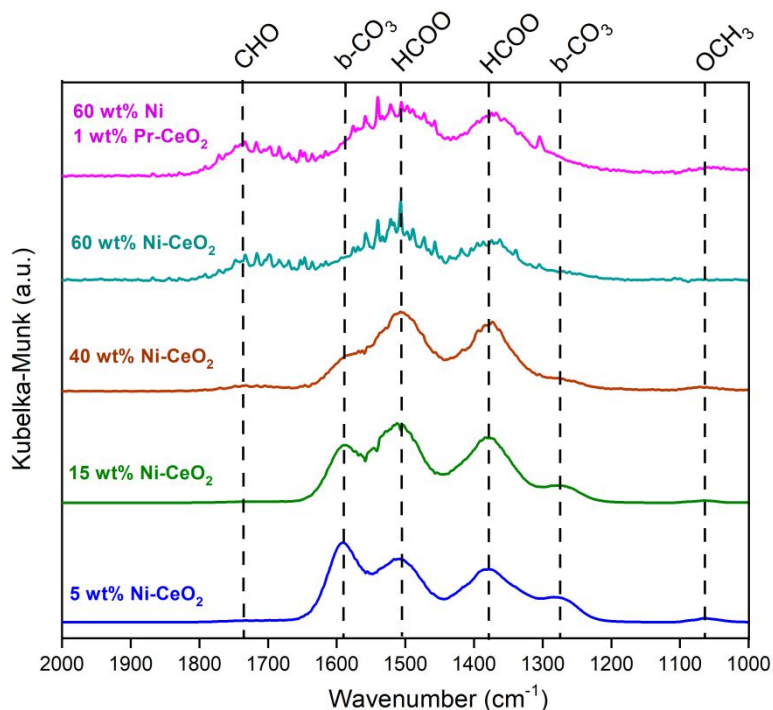

Fig 4. *In situ* DRIFTS for CO_2 methanation over 5 to 60 wt% $Ni-CeO_2$ and 60 wt% Ni 1 wt% $Pr-CeO_2$ at 250°C.

A proposed CO_2 methanation reaction mechanism derived from the experimental insights discussed above is illustrated in Scheme 1. Under reaction conditions, metallic Ni^0 sites (reduced prior to reaction) favor the dissociation of H_2 molecules, while oxygen vacancies generated at Ni-ceria interfaces facilitate the adsorption of CO_2 leading to the formation of bidentate carbonates (Step I). The adsorbed H atoms formed on metallic Ni spill over to the $Ni-CeO_x$ interfacial sites hydrogenating bidentate carbonate species to formates (Step II). The formates are further hydrogenated at the Ni/ceria interface to formyl species (Step III), a key intermediate in the CO_2

methanation mechanism via formate pathway. The formyl species can further undergo sequential hydrogenation reactions to form methane and water (Step IV).
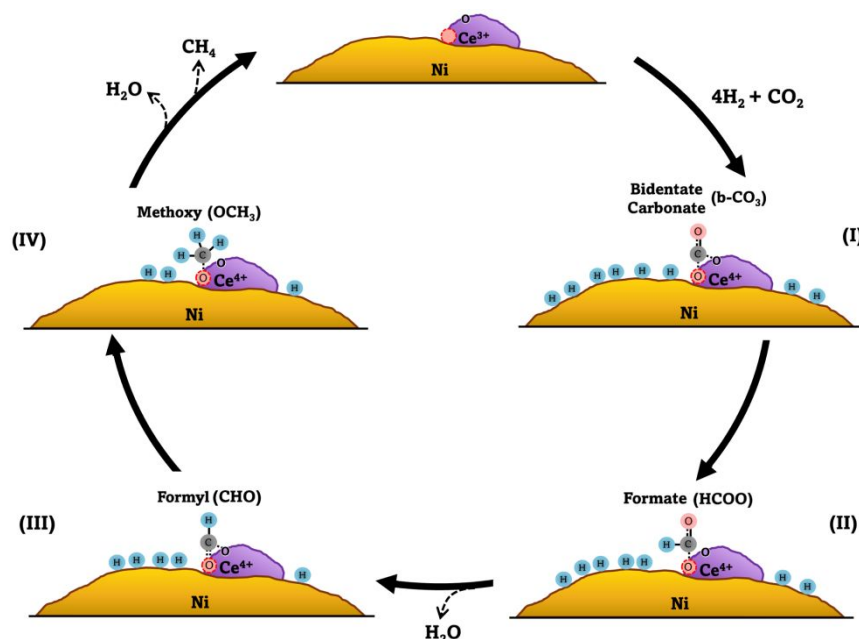
Scheme 1. Proposed CO_2 methanation reaction mechanism for inverse Ni-CeO$_x$ catalysts via a formate formation route.

4. Conclusion

Herein, we interrogated the effect of catalyst structure in Ni-CeO$_2$ catalysts and doping with aliovalent rare-earth metals on their catalytic activity, selectivity, and stability for CO_2 methanation. To elucidate the influence of Ni-CeO$_2$ interface, supported and inverse catalysts were synthesized by a co-precipitation method and evaluated through CO_2 methanation reactor kinetics and *in situ* DRIFTS studies. The inverse catalyst structures characterized by dispersed CeO$_2$ islands on large Ni particles exhibited the highest activity and selectivity towards CO_2 methanation, which correlated with an increase in the oxygen defect structure of ceria at the interface with Ni. This suggested that the defected ceria/Ni interface played an important role in CO_2 activation and the stabilization of intermediates that led to methane production. The concentration of oxygen defects in ceria was further tuned by doping the catalyst with aliovalent metals (Pr, Gd, La). It was found that doping the best performing inverse catalyst with 1 wt% of Pr increased the activity and selectivity to methane by increasing the concentration of oxygen vacancies in ceria. *In situ* DRIFTS studies showed that CO_2 methanation over the best performing

inverse Ni-CeO$_2$ catalyst structures occurred through a formate reaction pathway. The insights obtained through catalyst performance and characterization studies indicate that (i) the defected ceria/Ni interface plays an important role in improving catalyst performance for CO$_2$ methanation, and (ii) oxygen defects at the ceria/Ni interface could be tuned through engineering the metal-metal oxide structure and incorporation of aliovalent metal dopants.

Author contributions

The conceptualization and formal analysis were initiated by **Justin Borrero-Negrón**, **Yomaira Pagán-Torres**, and **Eranda Nikolla** and catalyst synthesis was accomplished by **Jesús Meléndez-Gil**. The catalyst characterization and kinetic studies were acquired, analyzed, curated, visualized, and validated by **Samiha Bhat** and **Miguel Sepúlveda-Pagán**, respectively. The original paper was drafted by **Samiha Bhat**, **Miguel Sepúlveda-Pagán, Justin Borrero-Negrón,** and **Jesús Meléndez-Gil**. **Yomaira Pagán-Torres** and **Eranda Nikolla** assisted in critical edits and revisions of the manuscript. All authors contributed equally on all aspects and approved the final manuscript.

Conflict of Interests

The authors declare that they have no known competing financial interests or personal relationships that could have appeared to influence the work reported in this paper.

Acknowledgements

Footnotes

Electronic supplementary information (ESI) available.

References

1 N. Mac Dowell, P. S. Fennell, N. Shah and G. C. Maitland, *Nat. Clim. Change*, 2017, **7**, 243–249.

2 P. Gabrielli, M. Gazzani and M. Mazzotti, *Ind. Eng. Chem. Res.*, 2020, **59**, 7033–7045.

3 M. a. A. Aziz, A. A. Jalil, S. Triwahyono and A. Ahmad, *Green Chem.*, 2015, **17**, 2647–2663.

4 S. Abanades, H. Abbaspour, A. Ahmadi, B. Das, M. A. Ehyaei, F. Esmaeilion, M. El Haj Assad, T. Hajilounezhad, D. H. Jamali, A. Hmida, H. A. Ozgoli, S. Safari, M. AlShabi and E. H. Bani-Hani, *Int. J. Environ. Sci. Technol.*, 2022, **19**, 3377–3400.

5 P. E. Hintze, A. J. Meier, M. G. Shah and R. DeVor, *Int. Conference on Environmental Systems*, 2018, **155**.

6 P. Frontera, A. Macario, M. Ferraro and P. Antonucci, *Catalysts*, 2017, **7**, 59.

7 J. Ashok, S. Pati, P. Hongmanorom, Z. Tianxi, C. Junmei and S. Kawi, *Catal. Today*, 2020, **356**, 471–489.

8 T. Sakpal and L. Lefferts, *J. Catal.*, 2018, **367**, 171–180.

9 S. Tada, T. Shimizu, H. Kameyama, T. Haneda and R. Kikuchi, *Int. J. Hydrog. Energy*, 2012, **37**, 5527–5531.

10 Y. Zhao, V. Girelli, O. Ersen and D. P. Debecker, *J. Catal.*, 2023, **426**, 283–293.

11 J. Lin, C. Ma, Q. Wang, Y. Xu, G. Ma, J. Wang, H. Wang, C. Dong, C. Zhang and M. Ding, *Appl. Catal. B Environ.*, 2019, **243**, 262–272.

12 R.P. Ye, Q. Li, W. Gong, T. Wang, J. J. Razink, L. Lin, Y.Y. Qin, Z. Zhou, H. Adidharma, J. Tang, A. G. Russell, M. Fan and Y.G. Yao, *Appl. Catal. B Environ.*, 2020, **268**, 118474.

13 L. Shen, J. Xu, M. Zhu and Y.F. Han, *ACS Catal.*, 2020, **10**, 14581–14591.

14 L. P. L. Gonçalves, J. Mielby, O. S. G. P. Soares, J. P. S. Sousa, D. Y. Petrovykh, O. I. Lebedev, M. F. R. Pereira, S. Kegnæs and Y. V. Kolenko, *Appl. Catal. B Environ.*, 2022, **312**, 121376.

15 W. L. Vrijburg, J. W. A. van Helden, A. Parastaev, E. Groeneveld, E. A. Pidko and E. J. M. Hensen, *Catal. Sci. Technol.*, 2019, **9**, 5001–5010.

16 M. D. Porosoff and J. G. Chen, *J. Catal.*, 2013, **301**, 30–37.

17 Y. Xie, J. Chen, X. Wu, J. Wen, R. Zhao, Z. Li, G. Tian, Q. Zhang, P. Ning and J. Hao, *ACS Catal.*, 2022, **12**, 10587–10602.

18 T. A. Le, M. S. Kim, S. H. Lee, T. W. Kim and E. D. Park, *Catal. Today*, 2017, **293–294**, 89–96.

19 S. M. Lee, Y. H. Lee, D. H. Moon, J. Y. Ahn, D. D. Nguyen, S. W. Chang and S. S. Kim, *Ind. Eng. Chem. Res.*, 2019, **58**, 8656–8662.

20 N. Rui, X. Zhang, F. Zhang, Z. Liu, X. Cao, Z. Xie, R. Zou, S. D. Senanayake, Y. Yang, J. A. Rodriguez and C.J. Liu, *Appl. Catal. B Environ.*, 2021, **282**, 119581.

21 Z. Hao, J. Shen, S. Lin, X. Han, X. Chang, J. Liu, M. Li and X. Ma, *Appl. Catal. B Environ.*, 2021, **286**, 119922.

22 G. Varvoutis, M. Lykaki, S. Stefa, V. Binas, G. E. Marnellos and M. Konsolakis, *Appl. Catal. B Environ.*, 2021, **297**, 120401.

23 M. Li, H. Amari and A. C. van Veen, *Appl. Catal. B Environ.*, 2018, **239**, 27–35.

24 C. Mebrahtu, S. Abate, S. Chen, A. F. Sierra Salazar, S. Perathoner, F. Krebs, R. Palkovits and G. Centi, *Energy Technol.*, 2018, **6**, 1196–1207.

25 M. Xiong, Z. Gao and Y. Qin, *ACS Catal.*, 2021, **11**, 3159–3172.

26 K. Chang, H. Zhang, M. Cheng and Q. Lu, *ACS Catal.*, 2020, **10**, 613–631.

27 F. Hu, R. Ye, Z.H. Lu, R. Zhang and G. Feng, *Energy Fuels*, 2022, **36**, 156–169.

28 Y. Guo, S. Mei, K. Yuan, D.J. Wang, H.C. Liu, C.H. Yan and Y.W. Zhang, *ACS Catal.*, 2018, **8**, 6203–6215.

29 P. Steiger, O. Kröcher and D. Ferri, *Appl. Catal. Gen.*, 2020, **590**, 117328.

30 J. Ren, C. Mebrahtu, L. van Koppen, F. Martinovic, J. P. Hofmann, E. J. M. Hensen and R. Palkovits, *Chem. Eng. J.*, 2021, **426**, 131760.

31 B. Post, *X-Ray Spectrom.*, 1975, **4**, A18–A18.

32 S. Zhang, J. Lee, D. H. Kim and T. Kim, *Catal. Sci. Technol.*, 2020, **10**, 2359–2368.

33 Z. Xiao, Y. Li, F. Hou, C. Wu, L. Pan, J. Zou, L. Wang, X. Zhang, G. Liu and G. Li, *Appl. Catal. B Environ.*, 2019, **258**, 117940.

34 C. Italiano, J. Llorca, L. Pino, M. Ferraro, V. Antonucci and A. Vita, *Appl. Catal. B Environ.*, 2020, **264**, 118494.

35 R. K. Singha, A. Shukla, A. Yadav, L. N. Sivakumar Konathala and R. Bal, *Appl. Catal. B Environ.*, 2017, **202**, 473–488.

36 Y. Yu, Z. Bian, J. Wang, Z. Wang, W. Tan, Q. Zhong and S. Kawi, *Catal. Today*, 2023, **424**, 113345.

37 Z. Xiao, S. Ji, F. Hou, Y. Li, H. Zhang, L. Wang, X. Zhang, G. Liu, J. Zou and G. Li, *Catal. Today*, 2018, **316**, 78–90.

38 L. Li, F. Chen, J.Q. Lu and M.F. Luo, *J. Phys. Chem. A.,* 2011, **115**, 27, 7972–7977.

39 H. Zheng, W. Liao, J. Ding, F. Xu, A. Jia, W. Huang and Z. Zhang, *ACS Catal.* 2022, **12**, 24, 15451–15462.

40 A. Ruiz Puigdollers, P. Schlexer, S. Tosoni and G. Pacchioni, *ACS Catal.*, 2017, **7**, 6493–6513.

41 E. W. McFarland and H. Metiu, *Chem. Rev.*, 2013, **113**, 4391–4427.

42 Z. Hu and H. Metiu, *J. Phys. Chem. C*, 2011, **115**, 17898–17909.

43 M. Guo, J. Lu, Y. Wu, Y. Wang and M. Luo, *Langmuir*, 2011, **27**, 3872–3877.

44 S. L. Rodríguez, A. Davó-Quiñonero, J. Juan-Juan, E. Bailón-García, D. Lozano-Castelló and A. Bueno-López, *J. Phys. Chem. C*, 2021, **125**, 12038–12049.

45 X. Xu, L. Liu, Y. Tong, X. Fang, J. Xu, D. Jiang and X. Wang, *ACS Catal.*, 2021, **11**, 5762–5775.

46 A. M. D'Angelo and A. L. Chaffee, *ACS Omega*, 2017, **2**, 2544–2551.

47 A. Cárdenas-Arenas, A. Quindimil, A. Davó-Quiñonero, E. Bailón-García, D. Lozano-Castelló, U. De-La-Torre, B. Pereda-Ayo, J. A. González-Marcos, J. R. González-Velasco and A. Bueno-López, *Appl. Catal. B Environ.*, 2020, **265**, 118538.

48 M. Zhu, P. Tian, X. Cao, J. Chen, T. Pu, B. Shi, J. Xu, J. Moon, Z. Wu and Y.F. Han, *Appl. Catal. B Environ.*, 2021, **282**, 119561.